Published in final edited form as:
Microporous Mesoporous Mater. 2015 January 1; 201: 151–159. doi:10.1016/j.micromeso.2014.09.012.

Zeolite Y Adsorbents with High Vapor Uptake Capacity and Robust Cycling Stability for Potential Applications in Advanced Adsorption Heat Pumps

Xiansen Li[a,*], **Shankar Narayanan**[a], **Vladimir K. Michaelis**[b,c], **Ta-Chung Ong**[b,c], **Eric G. Keeler**[b,c], **Hyunho Kim**[a], **Ian S. McKay**[a], **Robert G. Griffin**[b,c], and **Evelyn N. Wang**[a,*]

[a]Department of Mechanical Engineering, Massachusetts Institute of Technology, 77 Massachusetts Ave., Cambridge, Massachusetts 02139, USA

[b]Department of Chemistry, Massachusetts Institute of Technology, 77 Massachusetts Ave., Cambridge, Massachusetts 02139, USA

[c]Francis Bitter Magnet Laboratory, Massachusetts Institute of Technology, 77 Massachusetts Ave., Cambridge, Massachusetts 02139, USA

Abstract

Modular and compact adsorption heat pumps (AHPs) promise an energy-efficient alternative to conventional vapor compression based heating, ventilation and air conditioning systems. A key element in the advancement of AHPs is the development of adsorbents with high uptake capacity, fast intracrystalline diffusivity and durable hydrothermal stability. Herein, the ion exchange of NaY zeolites with ingoing Mg^{2+} ions is systematically studied to maximize the ion exchange degree (IED) for improved sorption performance. It is found that beyond an ion exchange threshold of 64.1%, deeper ion exchange does not benefit water uptake capacity or characteristic adsorption energy, but does enhance the vapor diffusivity. In addition to using water as an adsorbate, the uptake properties of Mg,Na-Y zeolites were investigated using 20 wt.% MeOH aqueous solution as a novel anti-freeze adsorbate, revealing that the MeOH additive has an insignificant influence on the overall sorption performance. We also demonstrated that the labscale synthetic scalability is robust, and that the tailored zeolites scarcely suffer from hydrothermal stability even after successive 108-fold adsorption/desorption cycles. The samples were analyzed using N_2 sorption, $^{27}Al/^{29}Si$ MAS NMR spectroscopy, ICP-AES, dynamic vapor sorption, SEM, Fick's 2nd law and D-R equation regressions. Among these, close examination of sorption isotherms for H_2O and N_2 adsorbates allows us to decouple and extract some insightful information underlying the complex water uptake phenomena. This work shows the promising performance of our modified zeolites that can be integrated into various AHP designs for buildings, electronics, and transportation applications.

*Corresponding author. Tel: +1 617 324 3311; Fax: +1 617 258 9346. xsli@mit.edu (X. Li); enwang@mit.edu (E.N. Wang).

Keywords

Adsorption heat pump; Zeolite; Ion exchange; Vapor uptake; Anti-freeze adsorbate

1. Introduction

Recent research on reversible AHPs has primarily focused on the development of more environment-friendly systems that can provide heating and cooling effects by utilizing low-grade thermal energy sources such as solar and geothermal energies or waste heat from a variety of industrial processes [1,2]. Although these studies involving a number of adsorbents have been well-documented for heating and cooling applications in stationary equipment or residential buildings [3–5], one of the key challenges is the development of more compact and modular AHPs that do not sacrifice their performance. In particular, an emerging field of application is for transportation systems including hybrid and electric vehicles [6], for which AHPs could extend the driving range by minimizing the electric battery power drainage, as compared to current systems which typically employ vapor compression cycles or resistive heaters, depending on the environmental condition. For the practical implementation of this adsorption based system, adsorbents must be developed with high vapor uptake capacities to maximize heating and cooling efficiencies as well as rapid adsorption/desorption kinetics for timely discharge and recharge. Additionally, parasitic energy consumption such as pumping power has to be minimized as well. The successful implementation of this technology can also be broadly applied for other transportation systems as well as residential and commercial buildings, whereby electricity consumption can be reduced during peak demand. Furthermore, with the use of ecobenign adsorbates instead of ozone-depleting fluorocarbon refrigerants, the negative environmental impact can be potentially mitigated.

A variety of adsorbents including zeolites, zeotypes, ordered mesoporous materials and metal-organic frameworks (MOFs) have been explored for AHP applications [1,2,7–14]. Zeolites and zeotypes are a family of microporous materials with tunable hydrophilicity/hydrophobicity, high surface area, uniform pore size distribution, interconnected pore/channel system, accessible pore volume, high adsorption capacity, ion-exchange capability and shape/size selectivity that can act as effective ion exchangers, catalysts, catalyst supports and adsorbents, *etc.* [15]. As compared to mesoporous materials and MOFs, a vast majority of hydrophilic zeolites or zeotypes have better thermal and hydrothermal stability, and exhibit typical Type I sorption isotherms based on the IUPAC classification, an important characteristic to maximize adsorption capacity even in very dilute dynamic vapor streams (*e.g.*, ~2% RP in this study). Therefore, the pumping power for delivering continuous vapor flow in the whole AHP systems can be reduced or even eliminated in favor of the coefficient of performance (COP) enhancement.

As far as the adsorbate is concerned, water has been widely used in AHPs owing to its high latent heat of condensation, small specific volume, hydrothermal stability and eco-friendly nature [16]. However, pure water as an adsorbate is undesirable due to freezing concerns during the chilly winters or harsh working conditions. To overcome this limitation, it is

necessary to select a suitable zeolite-compatible additive to the bulk water, allowing for freezing point (FP) depression at a relatively low dosing concentration but not at the cost of overall adsorption performance of adsorbents. Furthermore, since AHPs are more effective for heating than for cooling if the *T* differential is held equal, an additive that can contribute to the cooling efficiency and total vapor RP elevation should be another consideration.

In this contribution, we investigated in detail the effect of post-synthetic ion exchange treatment of NaY zeolites with ingoing Mg^{2+} cations on their vapor uptake properties. A number of fundamental parameters necessary for AHP design and other zeolite-related research were determined both experimentally and theoretically. In addition to investigating pure water and methanol as adsorbates, 20 wt.% MeOH aqueous solution as an anti-freeze adsorbate was examined on Mg,Na-Y zeolites in terms of sorption capacity and kinetics. Moreover, the cycling stability and bench-top synthetic scalability of these modified zeolites were evaluated.

2. Experimental

2.1. Synthesis

The parent Y-type Zeolite No. 1 was procured from Zeolyst Corp. in the Na^{+} form (CBV100).

2.1.1. Preparation of No. 2—No. 1 zeolites were ion exchanged twice with 1 M aqueous solution of magnesium nitrate (Sigma-Aldrich) each for 12 hrs at 80 °C under intense stirring with a solution volume/zeolite mass ratio of 20 ml/g. The resulting Mg^{2+}-exchanged Y No. 2 zeolites were isolated by centrifugation, decantation and then dispersion in deionized (DI) water. The procedure of aqueous rinse was repeated 3 times. Finally, the collected powders (6.25 g) were allowed to dry at 110 °C overnight.

2.1.2. Preparation of No. 3—Before a 3rd Mg^{2+}-ion exchange of No. 2 at 80 °C for 12 hrs (a solution/solid ratio = 40 ml/g), it was calcined in a quartz tube electrical furnace at 500 °C for 4 hrs with heating and cooling rates of 1 and 1.5 °C/min, respectively, under a flowing Ar atmosphere (80 ml/min) to facilitate the migration of Mg^{2+} ions into the small cages of the Y zeolites.

2.1.3. Preparation of No. 4—As a control experiment, No. 2 zeolites subjected further to the aforementioned calcination treatment alone were herein referred to as No. 4.

2.1.4. Preparation of No. 5—To explore the lab-scale synthetic scalability and reproducibility from batch to batch, a total of 52.5 g of Mg^{2+}-exchanged Y Zeolite No. 5 was prepared by following the protocol of No. 3 except for utilizing much larger synthesis facilities.

2.2. Cyclic lifetime assessment of No. 5

Small amounts of zeolite sample No. 5 were packed onto an aluminum block cartridge heater mounted in a closed plastic desiccator whose bottom was loaded with adequate DI water. During automated adsorption/desorption cycles, the zeolites were situated in a

variable water vapor pressure environment, depending on the ambient *T* within the closed desiccator. One *T*-programmed sequential cycle encompassed raising the heater *T* from 30 to 250 °C with a ramping duration of 1 hr, soaking at 250 °C for 1 hr, then cooling down to 30 °C within 1 hr, and finally re-soaking at 30 °C for 1 hr. Two series of cycles (50× and 108×) were carried out to assess their long-term hydrothermal stability.

2.3. Characterization techniques

2.3.1 Gas sorption analysis—Gas sorption studies were conducted to investigate the impact of ion exchange on the textural properties of these zeolites. The N_2 sorption measurements were performed at −196 °C using an automated gas sorption analyzer (Autosorb iQ_2, Quantachrome). Before the adsorption runs, each sample was degassed under vacuum (ca. 0.0014 Torr) at 370 °C for 12 h, and subsequently a compatible glass rod filler was rapidly inserted in the specimen cell to minimize the cell dead void. The BET (Brunauer, Emmett and Teller) surface area, S_{BET}, was obtained by applying the BET equation to a relative pressure (RP, P/P_0) range of 5–30% on the adsorption branch. The total pore volume, V_t, was evaluated from the adsorbed N_2 amount at a maximal RP of 95%. The *t*-plot method was used to differentiate between microporosity and mesoporosity. The micropore volume, V_{micro}, was determined by applying the *t*-plot method to an RP range of 20–50% on the adsorption branch of the isotherms. The slope of the *t*-plot (*V/t*) is equal to the external area, *i.e.*, the area of those pores which does not belong to micropores [17]. Multilayered adsorption phenomena may take place in the mesopores, macropores and outer surface, whereas micropores which have already been filled cannot contribute to the adsorption process.

2.3.2. Solid-state nuclear magnetic resonance (ssNMR)—^{27}Al and ^{29}Si MAS NMR experiments were respectively performed using 16.4 T (700 MHz, ^{1}H) and 9.4 T (400 MHz, ^{1}H) magnets each equipped with a home-built NMR spectrometer (courtesy of Dr. D. Ruben, FBML-MIT). Both spectra were respectively referenced with respect to 1 M $Al(NO_3)_3$ solution (0 ppm) and neat TMS (0 ppm) [18]. All acquired spectra were processed using RNMRP data processing software (courtesy of Dr. D. Ruben, FMBL-MIT). ^{27}Al spectra were acquired using a 3.2 mm Chemagnetics triple-resonance probe double tuned to ^{27}Al/^{1}H, and ^{29}Si data were acquired with a 3.2 mm home-built double resonance (^{29}Si/^{1}H) probe. Zeolites were ground using an agate mortar and pestle under dry N_2 gas and packed into a 3.2 mm (o.d.) ZrO_2 rotors (~26 μl fill volume). The magic angle within the probe was set using the ^{79}Br resonance of solid KBr and shimmed using adamantane prior to signal acquisition.

^{27}Al MAS NMR spectra ($\omega_L/2\pi$ = 223 MHz) were acquired using a Bloch [19] experiment with a short quantitative tip angle (15°, ^{11}B $\gamma B_1/2\pi$ = 50 kHz), a spinning frequency of 16 kHz ($\omega_r/2\pi$) as well as between 8,192 and 64,384 co-added transients. ^{29}Si MAS NMR spectra ($\omega_L/2\pi$ = 78 MHz, ^{29}Si $\gamma B_1/2\pi$ = 50 kHz) were acquired using either Bloch or Hahn-echo [20] experiment, a spinning frequency of 10 kHz, 3,072 co-added transients, and a recycle delay of 60 s. All data were acquired with high-power (^{1}H $\gamma B_1/2\pi$ = 83 kHz) two-pulse phase modulation (TPPM) ^{1}H decoupling during acquisition.

2.3.3. Elemental analysis (EA)—EA was conducted at the MIT Center for Materials Science and Engineering-Shared Experimental Facility (CMSE-SEF) using a Horiba Jobin Yvon ACTIVA-S inductively coupled plasma-atomic emission spectrometer (ICP-AES). Calibration solutions of specific concentrations were prepared from ICP standard solutions purchased from Sigma-Aldrich for Si, Al and Mg elements, and from Ricca Chemical Company for Na element.

2.3.4. Dynamic vapor sorption (DVS) analysis—Adsorption/desorption properties of various zeolites were evaluated by an automated vapor sorption analyzer (DVS Vacuum, Surface Measurement Systems Ltd.) in typical ranges of vapor RP (1–90%) and *T* (25–65 °C). The analyzer measured the uptake and loss of vapor gravimetrically using a delicate SMSUltraBalance with a mass sensitivity of 0.1 μg. The RP surrounding the sample was controlled by using a mass flow controller. The temperature (*T*) was maintained constant (±0.1 °C) by enclosing the manifold in a *T*-controlled incubator. The zeolite powdery sample (ca. 30 mg) was loaded into the specimen pan and then placed into the instrument. Prior to being exposed to any vapor flow, the sample was degassed *in situ* at 370 °C under vacuum (~10^{-5} Torr) for 8–12 hrs to desorb any physisorbed moisture. Afterwards, the sample was exposed to the desired RP and the vapor uptake was monitored under dynamic vapor flow. A series of equilibrium points were acquired by directly measuring the sample weight variation in response to a stepwise RP change.

2.3.5. Scanning electron microscopy (SEM)—The morphology and particle size of the pristine and tailored Y-type zeolites were observed by an Analytical Scanning Electron Microscope (JEOL-6010LA) at an accelerating voltage of 10 or 15 kV. A gold film was sputter-coated onto these samples before imaging.

3. Results and Discussion

3.1. N_2 sorption analyses

Fig. 1 shows N_2 sorption isotherms of the parent and modified Y zeolites, and the corresponding textural parameters are presented in Table 1. As illustrated in Fig. 1, all the samples exhibit Type I sorption isotherms without noticeable hysteresis loops, characteristic of the adsorption on microporous materials. As a result, such post treatments as multiple ion exchanges and calcination do not lead to the significant structural degradation primarily associated with the dealumination phenomena. Relative to the reference No. 1, a remarkable alteration of textural parameters is identified on the doubly exchanged Zeolite No. 2 (Table 1). All variables of No. 3 prepared by extra calcination, followed by a 3rd ion exchange are further improved to different extents over No. 1, *e.g.*, with an increase in V_{micro} by 5%, which can be interpreted by the smaller occupied volume of Mg^{2+} than Na^{+} and altered zeolite density. Nevertheless, the extent of incremental improvement of these parameters arising from extra tailoring of No. 3 tends to level off with respect to No. 2, thus predicting the proximity to steady-state Mg^{2+} ion exchange. It is worth noting that $S_{external}$ increases by as much as 34.5% as a consequence of the double ion exchange, and is weakly dependent on extra treatment. Basically, it is the microporosity that dictates the vapor uptake capacity at a low RP rather than the external porosity (*i.e.*, mesoporosity).

3.2. ^{27}Al/^{29}Si magic-angle spinning NMR (MAS NMR)

Sato *et al.* reported that combined NH_4^+ ion exchange with calcination could lead to irreversible structural changes of NaY zeolites with different framework Si/Al ratios linked to dealumination and concurrent mesoporosity formation [21]. To probe the structural changes within our Y-type zeolites, all ^{27}Al MAS NMR spectra (Fig. 2) with chemical shifts sensitive to the Al coordination environments (*i.e.*, $^{[4]}$Al, $^{[5]}$Al and $^{[6]}$Al species) were acquired under high-fields (16.4 T) and moderately fast MAS conditions in order to minimize the quadrupolar coupling effects [22,23]. ^{27}Al MAS NMR spectra show an intense four-coordinate Al ($^{[4]}$Al) resonance assigned to Al in the zeolite framework with a chemical shift (δ_{cgs}) of 62 ppm, which is consistent with other reports of NaY zeolites [24,25]. The symmetric and narrow $^{[4]}$Al resonance with an isotropic chemical shift (δ_{iso}) of 63 ppm (~700 Hz in full-width at half-maximum) has an experimentally determined quadrupolar coupling constant (C_Q) of 2 MHz, accounting for the quadrupole-induced shift. For all three zeolites, the ^{27}Al spectra show > 99% framework Al species. As presented in Table 2, a small fraction of extra-framework six-coordinate Al ($^{[6]}$Al) species (< 0.3%, ~0 ppm) is present in the sample No. 3. Minor dealumination of No. 3 is in good agreement with N_2 sorption analyses (*vide supra*). This dealumination is mainly attributed to the calcination given that the integrity of No. 2 remains intact after double ion exchanges.

^{29}Si MAS NMR has been used to identify the Si(*n*Al) medium-range ordering as an acceptable tool for quantifying the framework Si/Al ratio of Al-rich zeolites [26–28]. ^{29}Si MAS NMR spectra (79 MHz, ^{29}Si) are shown in Fig. 3 for Nos. 1, 2 and 3, indicating well-resolved Si(*n*A1) resonances where *n* (*n* = 0–4) is the number of Al atoms linked to $^{[4]}$Si *via* oxygen bridges to the central Si atom. The four resonances are assigned to Si(3Al), Si(2Al), Si(1Al) and Si(0A1) units with the isotropic chemical shifts of −89, −94, −100 and −105 ppm, respectively, as found in Ref. [29]. Deconvoluting the resonances gives a framework Si/Al ratio of ~2.5 (Table 2), which is comparable to several typical Y-type zeolites [22,24,25,]. As expected, upon increasing the steps of treatment, both peak symmetry and resolution of these four resonances turn out to degrade, suggesting distorted local Si environments due to polarization from the closest highly charged extra-framework Al species.

3.3. Elemental analyses

It is well-known that exhaustive ion exchange of Na^+ with Mg^{2+} from Y-type zeolites without any concomitant structural disintegration has posed a grand challenge until now [30]. In general, approximately 30% of the Na^+ ions residing in small cages (sodalite cages and hexagonal prisms) cannot be readily exchanged under conventional hydrothermal exchange conditions. This result is anticipated because both hydrated Mg^{2+} and Na^+ ions are too bulky to diffuse through the 6-membered-ring (6MR) windows with a free diameter of 2.5 Å that are the entrances to these small cages. Moreover, more energy is required to strip the hydration shell from the smaller Mg^{2+} cations. To quantify the ion exchange degree (IED), the bulk elemental composition of the zeolites based on ICP technique is presented in Table 2. From ICP analysis, the bulk Si/Al and Na^+/Al ratios of No. 1 are 1.95 and 1.15, respectively. The residual NaOH originating from the preceding hydrothermal preparation in alkaline media is responsible for the Na^+/Al ratio slightly greater than unity. The doubly

exchanged No. 2 zeolites yield an IED of 64.1%, whereas that of 71.5% is accomplished for No. 3, which is in line with the well-established IED for FAU-type zeolites [31]. During calcination of the zeolites at 500 °C for 4 hrs, an inter-cage ion exchange between Na^+ and Mg^{2+} ions could take place, thus slightly enhancing the IED. It is worth noting that there are small deviations in the measured Si/Al ratio between the ICP and NMR methods (Table 2), as encountered by other researchers [32,33]. The exact reason for these small discrepancies remains unclear. This technique of sequential exchange, calcination and re-exchange to produce low-Na^+ Y zeolites is also applicable for other cations provided that the inhibition from replacing Na^+ in the small cages is not due to the bare ion size of the ingoing cations. On the other hand, the co-generation of trace amounts of protons is observed presumably due to the over-washing of zeolites in between ion exchanges and to the slight hydrolysis of the exchanged Mg^{2+} ions caused by polarizing adsorbed water in the strong electrostatic field between the exchanged cations and the framework $[AlO_2]^-$ anions [34]. Hydrolytic cleavage of the Si-O-Al bonds frequently occurs at these protonated sites in the zeolite framework, leading to the undesirable dealumination under steaming conditions [35]. As a consequence, multiple exchanges in conjunction with calcination lead to gradual leaching of some labile Al^{3+} species from the crystal lattice (Table 2).

3.4. Dynamic vapor sorption analyses

3.4.1. Water uptake performance—For NaY zeolites exchanged with divalent Mg^{2+} cations, one could expect a higher adsorption capacity than with Na^+ because two Na^+ cations are simultaneously replaced by a single Mg^{2+} while ignoring the potential hydrolysis of Mg^{2+}. Meanwhile, the ionic radius of Mg^{2+} (0.66 Å) is smaller than that of Na^+ (0.97 Å). Therefore, the net volume occupancy by these Mg^{2+} ions should be less than one third as with Na^+. On the other hand, the electrostatic field strength inside the zeolite channels and cavities would be enhanced as a result of increased effective electric charge of ingoing Mg^{2+} cations. Water sorption isotherms of No. 1, Nos. 2 and 4, as well as No. 3 as functions of *T* and RP are shown in Fig. 4 A, B and C, respectively, whereas Table 3 lists the representative uptake capacities and *Ds* at the working RP of 2%. Except for the isotherms of No. 1 that show hysteresis loops stemming from the smaller *D* of desorption, all of the other sorption profiles exhibit quite similar Type I isotherms, an attribute of microporous zeolites. Within the narrow *T* interval under study, the uptake capacity is weakly *T* dependent at a fixed RP, but is a function of RP. Nevertheless, it is worth noting that the uptake amount in the low RP regime is a little more sensitive to *T* than that in the high RP range since adsorption phenomena on zeolites are strongly exothermic processes with isosteric heats of adsorption highly dependent on the sorbate surface coverage. As expected, ion exchange is one of the most straightforward and robust ways to effectively boost the uptake amount, especially in the low RP region (Table 3). The uptake comparison between Nos. 2 and 3 indicates that a slightly deeper IED does not have a favorable effect on the uptake capacity, which can be explained by the minute degree of dealumination, the exchange-induced Al leaching and a small fraction of calcination-induced bare Mg^{2+} ion migration into water-inaccessible hexagonal prisms for the latter (Fig. 2 C and Table 2). It is found that calcination and protonated sites are two dominant factors of dealumination, yielding Zeolite No. 4 with the smallest water uptake at 2% RP and 25 °C among Nos. 2, 3 and 4 (Table 3). Conversely, as clearly shown in Fig. 4 C, the desorption *T* for zeolite adsorbents strongly affects the final

degree of regeneration. For instance, 6.1 wt.% of strongly bound water still remains entrapped inside the zeolite intracrystalline voids after the last desorption step at 65 °C under vacuum for 2 hrs without introducing any dynamic water vapor flow.

3.4.2. Intracrystalline diffusivity (D) and SEM observation—The charging/discharging kinetics of zeolites is as crucial as their adsorption capacity to achieve highly efficient AHP systems. Fick's 2nd law of diffusion (Eq. 1) describing non-steady-state mass transfer is used to determine *D*

$$\frac{\partial c}{\partial t}=D\frac{\partial^2 c}{\partial x^2} \quad (1)$$

For the purpose of measuring *D* in powdered zeolite samples, spherical geometry, constant *D* and constant source concentration are assumed, resulting in the following Eq. 2 in a spherical coordinate system

$$\frac{\partial c}{\partial t}=\frac{1}{r^2}\frac{\partial}{\partial r}(Dr^2\frac{\partial c}{\partial r}) \quad (2)$$

Using the additional boundary conditions of $m = 0$ at $t = 0$, $m = m_{equil.}$ at $t = \infty$, and $\partial c/\partial r = 0$ at $r = 0$ (*i.e.*, no concentration gradient at the center of the sphere), Eq. 2 has the following solution [36]

$$\frac{\mathrm{m}_t}{\mathrm{m}_{equil.}}=1-\frac{6}{\pi^2}\sum_{\mathrm{n}=1}^{\infty}\left(\frac{1}{\mathrm{n}^2}\right)\exp(-\frac{\mathrm{n}^2\pi^2 Dt}{r^2}) \quad (3)$$

where *r* is the particle radius. For short times, Eq. 3 can be simplified into

$$\frac{\mathrm{m}_t}{\mathrm{m}_{equil.}}=\frac{6}{r}\sqrt{\frac{Dt}{\pi}}(\frac{\mathrm{m}_t}{\mathrm{m}_{equil.}}<0.2) \quad (4)$$

$$\mathrm{or}\frac{\mathrm{m}_t}{\mathrm{m}_{equil.}}=\frac{6}{\mathrm{r}}\sqrt{\frac{Dt}{\pi}}-\frac{3Dt}{r^2}(0.2<\frac{\mathrm{m}_t}{\mathrm{m}_{equil.}}<0.8) \quad (5)$$

where $m_t/m_{equil.}$ is the ratio of the mass at a given time *t* to that at an infinite time (*i.e.*, equilibrium mass). For our analysis, Eq. 5 is chosen because it is valid over a wider range of $m_t/m_{equil.}$ values.

Second-order polynomial fitting of $m_t/m_{equil.}$ against $\sqrt{t}$ for Zeolite No. 3 at 25 °C and 2% RP is shown in Fig. 5, together with the corresponding sorption kinetics as a function of stepwise RP (inset). Upon exposure of the outgassed zeolite powders to the dynamically flowing water vapor stream, there is a steep increase in sample mass as a consequence of surface water adsorption (inset). This fast process is generally complete within ca. 10 min which is then followed only by water diffusion into the intracrystalline voids. This is the starting reference point from which the *D* is calculated ($m_0 = 0$ at $t = 0$). As the dynamic

adsorption progresses, the rate-limiting intracrystalline adsorption proceeds slowly until an equilibrium state is reached. This behavior also holds true for the adsorption occurring at other RP steps.

The particle size of these zeolites is estimated by SEM images (Fig. 6), demonstrating an average octahedral particle size of ~1 μm, regardless of the tailoring methodology. Based on this estimated particle size, the regression (Fig. 5) gives a D of 1.94×10^{-12} cm^2/s using the 1st-order coefficient of the polynomial fitted equation. The T-dependent Ds of the other zeolites are similarly calculated and summarized in Table 3 (regression curves not shown here for brevity). Both the 3D pore system and large-pore nature of FAU-type zeolites contribute to the appreciable Ds ranging from 10^{-13} to 10^{-12} cm^2/s, depending on the operating T and IED. An increase in D shown in Table 3 with testing T is expected since diffusion in the restricted geometries of zeolites is an activated transport process. In terms of IED dependency, the D rises with increasing IED due to the molecular traffic jam effect in the confined intracrystalline space of zeolites [37]. However, the D of No. 4 is an exception in regard to No. 2, which can be understood by a few locally occluded non-framework Al species extracted by calcination.

3.4.5. Characteristic adsorption energy—The performance of AHPs is strongly relevant to the adsorption heat released by the activated zeolite adsorbents. The classic Dubinin-Radushkevich (D-R) equation provides fundamental adsorption information specifically in the micropores, which takes the form [38]

$$V=V_0\exp[-(\frac{RT}{\beta E_0}\ln\frac{P_0}{P})^2] \quad (6)$$

where V represents the volume of adsorbate condensed in micropores at P/P_0 (1–20%) and T (condensed adsorbate can be roughly considered as liquid-like one); V_0 is the total volume of accessible micropores by a given adsorbate at 100% RP; E_0 is the characteristic adsorption energy of an adsorbate with respect to a given solid; and the affinity coefficient β is the ratio of the adsorption potential of the adsorbate relative to a reference adsorbate (*e.g.*, benzene). β is equal to 0.2 for water adsorbate.

The D-R plot of the No. 3 zeolites at 25 °C for water vapor uptake is shown in Fig. 7 as an example but with the other D-R fittings omitted here for brevity. The effects of T on the regression coefficient (R), V_0 and E_0 are summarized in Table 4, highlighting that both V_0 and E_0 are a weak function of T within the narrow T range of interest. After the linear D-R regression, the calculated V_0 is 0.375 ml/g along with an E_0 of −107.9 kJ/mol that is approximately 2.7 times the enthalpy of condensation for water (−40.7 kJ/mol). Obviously, the V_0 lies intermediate between V_{micro} (0.342 ml/g) and V_t (0.393 ml/g) both quantified by N_2 sorption analyses (Table 1). This means that water uptake at 100% RP takes place at three different locations inside Mg,Na-Y zeolites, *i.e.*, the small cages, supercages and external surfaces/partial interstitial voids. It is commonly accepted that water is sequentially adsorbed in FAU-type zeolites in three RP-dependent steps corresponding to the adsorption around the charge-compensating cations, monolayer adsorption and condensation in the supercages [39]. Nevertheless, our findings suggest that such a description is incomplete in

cases where the condensation in the nanoscale intercrystalline voids cannot be totally ignored near the saturation pressure provided that the $S_{external}$ proportion cannot be neglected (7.4% herein). In faujasite zeolites, the cations in the small cages (at sites SI, SI' and SII') [40] are sterically inaccessible to N_2 molecules (3.64 Å), and so only the supercage cations (at SII, SIII and SIII') are available to interact with the quadrupole moment of N_2. Instead, slim water molecules can have access to both small cages and supercages with an effective opening of 7.4 Å [41]. By comparing V_0 with V_{micro}, the adsorption quantity in the small cages takes up ~8.8% of the total uptake in the micropores assuming the density of adsorbed water to be 1 g/ml. With reference to V_t (Table 1), a maximal water uptake of 42.6 wt.% at 25 °C can be theoretically predicted over defect-free Mg,Na-Y zeolites (~70% IED) while extrapolating RP to ~100%, as experimentally corroborated in Ref. [42]. Furthermore, the monolayer-forming adsorption is already in close proximity to completion at ~1% RP considering the calculated monolayer adsorption volume of 0.279 ml/g based on a BET fitting of the water adsorption isotherm branch within 5–20% RP (not shown here). Capillary condensation in the interstitial voids initiates at ~69.3% RP, accounting for 12% of the total water adsorption amount at ~100% RP and 25 °C. On the other hand, as indicated in Table 4, the mean E_0 makes no significant difference between Nos. 2 and 3, which is compatible with their respective water uptake quantity. The E_0 of −105.2 kJ/mol on average is quite similar to the isosteric heats of adsorption at zero sorbate coverage of zeolites such as MgY [30], CuY [30], ZnY [30] and BaY [39] with water as the adsorbate. This result is reasonable since the D-R equation delivers the most effective solutions to the problems linked to the dilute vapor adsorption occurring in microporous materials. Ion exchange to a greater extent enables the mean E_0 of No. 3 to improve by 34.4% in comparison to the parent No. 1 zeolites because the hydration enthalpy of Mg^{2+} counterions (−1923 kJ/mol) is much larger than that of Na^+ ions (−418 kJ/mol). The tunability of E_0 could offer an attractive prospect for the creation of zeolite adsorbents with a high thermal energy storage density.

3.4.6. Vapor uptake performance for 20 wt.% MeOH/H_2O mixture—Pure water adsorbate in the evaporator and water reservoir may pose a significant risk of frosting or freezing in chilly winter seasons, thus disabling the operation of the AHPs. To circumvent this scenario, non-flammable 20 wt.% MeOH aqueous solutions are examined besides pure water. Several important physical variables of the mixed vapor adsorbate as a function of T are presented in Table 5 along with those of water and MeOH for comparison. The blending of water with 20 wt.% MeOH allows for the practice of AHPs at elevated total vapor pressure due to the lowered boiling point (BP) of the mixture (86 °C) and at depressed FP down to −18 °C. In this case, the evaporator can be smoothly operated at a lower T (*e.g.*, < 0 °C), thereby promising improved cooling efficiency. Additionally, no significant reduction in water vapor partial pressure is observed upon dosing MeOH additive, showing small decreases of 6.2, 4.6, 4.3% at 25, 45 and 65 °C, respectively. We thus infer that the mixed MeOH/H_2O adsorbate would not have a pronounced adverse impact on the water uptake properties of zeolites. The mixed and pure MeOH vapor uptake properties of No. 3 as functions of RP and T are shown in Fig. 8 and Table 6. Fig. 8 shows that the operational T has little influence on the total adsorption capacity for MeOH aqueous mixtures, as with water adsorbate (Fig. 4 C). By comparing the data in Tables 6 and 3, the uptake capacity is

nearly independent of adsorbate type. Meanwhile, the corresponding *Ds* at 2% RP for mixed vapor are slightly smaller than those for water vapor. As such, the water component plays a dominant role over MeOH in the competitive adsorption process, a favorable attribute in the pursuit of better-performing AHPs for chilly conditions.

3.4.7. Vapor uptake performance for MeOH—To further evaluate the effect of the MeOH additive on water uptake properties, the uptake of pure MeOH vapor by No. 3 was investigated at various RPs and *Ts* (Fig. 8 and Table 6). For MeOH uptake, the adsorption capacity counter-intuitively increases with rising *T*. The main reason for this trend is that the steady-state adsorption of MeOH cannot be fully fulfilled only within the RP-specific sorption intervals identical to those for either water or MeOH/H_2O mixture, originating from more sluggish mobility of MeOH (3.8–4.1 Å in kinetic diameter [43]) inside constrained spaces as opposed to water. The higher adsorption *T* favoring larger *D* promotes the faster approach towards the quasi-equilibrium of adsorption. Interestingly, upon desorption, an appreciable portion of MeOH molecules cannot be desorbed rapidly at low *T* despite the lower BP of MeOH compared to that of water. In this case, some MeOH molecules may condense with trace amounts of zeolite hydroxyl groups to form methoxyl entities [44] that are hardly removable at low *T* even under vacuum. Additionally, the exchanged Mg^{2+} ions probably in association with MeOH clusters to form stable $[Mg(CH_3OH)_n]^{2+}$ or $[MgOCH_3]^+$ adducts confined in the supercages are presumably another factor affecting the extent of desorption [45]. As shown in Table 6, the adsorption capacity of No. 3 for MeOH adsorbate is inferior to those for both water (Table 3) and MeOH/H_2O mixture, further lending support to the above reasoning regarding quite low MeOH loading in the adsorbed phase inside zeolites in relation to water constituent.

3.5. Synthetic scalability and cyclic stability

The adsorption/desorption cycling stability of zeolite adsorbents is critical to their practical viability in AHP systems. Sorption isotherms of Mg,Na-Y Zeolite No. 5 for water adsorbate at 25 and 65 °C before and after multiple cycles are plotted in Fig. 9 A and B, respectively. Comparison of the sorption isotherms of No. 3 (Fig. 4 C) and fresh No. 5 (Fig. 9 A) both at 25 °C manifests the robust synthetic reproducibility from batch to batch in terms of sorption capacity, independently of the bench-top preparative scale. After 50× cycles, the water uptake quantities measured at 25 °C only deteriorate from 31.16 down to 30.28 wt.% at 2% RP and from 37.90 down to 36.39 wt.% at 80% RP, whereas the corresponding degradations are respectively 7.2% from 31.16 to 28.92 wt.% and 6.2% from 37.90 to 35.54 wt.% after undergoing 108× cycles (Fig. 9). In contrast, after 108× cycles, degradation rates of only 2.05 and 4.5% at 2 and 80% RP, respectively, are observed while experimenting at 65 °C (Fig. 9 B). To gain some insights into the slight degradation in performance, N_2 sorption analyses are performed on No. 5 before and after 108× cycles (Fig. 10 and Table 1). After multiple cycles, there is a subtle loss of microporosity, as reflected by the variations in both V_{micro} and S_{micro}. The slight framework dealumination provoked by water attack at the cyclic *T* maximum of 250 °C is likely the major cause of the minor drop in these textural parameters, and consequently leads to the slight deterioration in water uptake capacity. Another influential factor is the agglomeration or sintering of micro-sized zeolite particles at elevated *T*, leading to a 45% decline in $S_{external}$ after 108× cycles. Nevertheless, sorption

kinetic trials reveal that the *D* of water vapor is rather susceptible to the number of structural defect sites and the extent of particle aggregation, both of which are responsible for the reduction in *D* by 15% at 65 °C and 2% RP (but still as much as 1.23×10^{-12} cm^2/s after 108× cycles). In summary, the Mg,Na-Y zeolites are proven to be hydrothermally stable against multiple adsorption/desorption cycles given the aggressive cycling conditions adopted here.

4. Conclusions

We demonstrated that Y-type zeolites finely tailored by ion exchange can bring about enhanced vapor uptake capacity, characteristic adsorption energy and intracrystalline diffusivity relative to the parent zeolites. It was also demonstrated that the sorption performance of the modified zeolites is not reduced significantly even with a 20 wt.% $MeOH/H_2O$ adsorbate instead of water adsorbate, a property that could lead to improved cooling efficiency of AHPs and more reliable AHP operation in cold climates. Both long-term cycling stability and synthetic scalability on a lab scale were confirmed in this study. A range of fundamental parameters presented here (*e.g.*, sorption capacity, diffusivity and characteristic adsorption energy) not only serve as a basis for future AHP materials optimization and design, but also contribute to advancing the basic understanding of FAU-type zeolites at a fundamental level. By presenting a superior sub-nanostructured porous material, this work offers a potential pathway towards the successful deployment of environmental-friendly and high-performance AHPs in existing vehicles, residential and commercial buildings.

Acknowledgments

This research was supported by the U.S. Department of Energy's Advanced Research Projects Agency-Energy under control No. 0471-1627 with Drs. Ravi Prasher and James Klausner as program managers. NMR studies were supported by the National Institute of Biomedical Imaging and Bioengineering of the National Institute of Health under award Nos. EB-001960 and EB-002026. V.K.M. is grateful to the Natural Sciences and Engineering Research Council of Canada for a Postdoctoral Fellowship. We thank Drs. Daniel J. Burnett and Vladimir Martis at Surface Measurement Systems Ltd. for valuable discussion.

References

1. Tchernev, DI. Natural Zeolites: Occurrence, Properties, Use. Sand, LB.; Mumpton, FA., editors. Vol. 45. Elmsford, New York and Oxford: Pergamon Press; 1978.
2. Janchen J, Ackermann D, Stach H, Brosicke W. Solar Energy. 2004; 76:339–344.
3. Dieng AO, Wang RZ. Renewable and Sustainable Energy Reviews. 2001; 5:313–342.
4. Demir H, Mobedi M, Ulku S. Renewable and Sustainable Energy Reviews. 2008; 12:2381–2403.
5. Xue B, Iwama Y, Tanaka Y, Nakashima K, Wijayanta AT, Nakaso K, Fukai J. Experimental Thermal and Fluid Science. 2013; 46:54–63.
6. Narayanan, S.; Li, X.; Yang, S.; McKay, I.; Kim, H.; Wang, EN. Proceedings of the ASME 2013 Heat Transfer Summer Conference; 2013. HT2013-17472.
7. Stach H, Mugele J, Janchen J, Weiler E. Adsorption. 2005; 11:393–404.
8. Tatlıer M, Erdem-Senatalar A. Micropor. Mesopor. Mater. 1999; 28:195–203.
9. Wojcik AMW, Jansen JC. Th. Maschmeyer, Micropor. Mesopor. Mater. 2001; 43:313–317.
10. Tatlıer M, Erdem-Senatalar A. Micropor. Mesopor. Mater. 2002; 54:89–96.
11. Bonaccorsi L, Calabrese L, Freni A, Proverbio E. Micropor. Mesopor. Mater. 2013; 167:30–37.

12. Bonaccorsi L, Freni A, Proverbio E, Restuccia G, Russo F. Micropor. Mesopor. Mater. 2006; 91:7–14.
13. Wade CR, Corrales-Sanchez T, Narayan TC, Dincă** M. Energy Environ. Sci. 2013; 6:2172–2177.
14. Furukawa H, Gándara F, Zhang Y-B, Jiang J, Queen WL, Hudson MR, Yaghi OM. J. Am. Chem. Soc. 2014; 136:4369–4381. [PubMed: 24588307]
15. Cundy CS, Cox PA. Chem. Rev. 2003; 103:663–701. [PubMed: 12630849]
16. Wongsuwan W, Kumar S, Neveu P, Meunier F. Applied Thermal Engineering. 2001; 21:1489–1519.
17. Lippens BC, de Boer JH. J. Catal. 1965; 4:319–413.
18. Harris RK, Becker ED. J. Magn. Reson. 2002; 156:323–326.
19. Bloch F. Phys. Rev. 1946; 70:460–475.
20. Hahn EL. Phys. Rev. 1950; 80:580–594.
21. Sato K, Nishimura Y, Matsubayashi N, Imamura M, Shimada H. Micropor. Mesopor. Mater. 2003; 59:133–146.
22. Fyfe CA, Bretherton JL, Lam LY. J. Am. Chem. Soc. 2001; 123:5285–5291. [PubMed: 11457391]
23. Fyfe CA, Bretherton JL, Lam LY. Chem. Commu. 2000; 17:1575–1576.
24. Klinowski J, Fyfe CA, Gobbi GC. J. Chem. Soc., Faraday Trans. 1. 1985; 81:3003–3019.
25. van Bokhoven JA, Roest AL, Koningsberger DC, Miller JT, Nachtegaal GH, Kentgens APM. J. Phys. Chem. B. 2000; 104:6743–6754.
26. Klinowski J, Thomas JM, Fyfe CA, Gobbi GC. Nature. 1982; 296:533–536.
27. Lippmaa E, Mägi M, Samoson A, Engelhardt G, Grimmer A-R. J. Am. chem. Soc. 1980; 102:4889–4893.
28. Lippmaa E, Mägi M, Samoson A, Tarmak M, Engelhardt G. J. Am. chem. Soc. 1981; 103:4992–4996.
29. Klinowski J, Thomas JM, Fyfe CA, Gobbi GC, Hartman JS. Inorg. Chem. 1983; 22:63–66.
30. Coughlan B, Carroll WM. J. Chem. Soc., Faraday Trans. 1. 1976; 72:2016–2030.
31. Sherry HS. J. Phys. Chem. 1968; 72:4086–4094.
32. Wu C, Chao K. J. Chem. Soc. Faraday Trans. 1995; 91:167–173.
33. Maruo T, Yamanaka N, Tsunoji N, Sadakane M, Sano T. Chem. Lett. 2014; 43:302–304.
34. Ward JW. J. Catal. 1968; 10:34–46.
35. Guisnet M, Wang QL, Giannetto G. Catal. Lett. 1990; 4:299–302.
36. Perry, RH.; Green, DW., editors. Perry's Chemical Engineers' Handbook. 7th Edition. McGraw-Hill; 1997.
37. Derouane EG, Gabelica Z. J. Catal. 1980; 65:486–489.
38. Nguyen C, Do DD. Carbon. 2001; 39:1327–1336.
39. Moise JC, Bellat JP, Methivier A. Micropor. Mesopor. Mater. 2001; 43:91–101.
40. Kim CW, Jung KJ, Heo NH, Kim SH, Hong SB, Seff K. J. Phys. Chem. C. 2009; 113:5164–5181.
41. Broussard L, Shoemaker DP. J. Am. Chem. Soc. 1960; 82:1041–1051.
42. Ng E-P, Mintova S. Micropor. Mesopor. Mater. 2008; 114:1–26.
43. ten Elshof JE, Abadal CR, Sekulic J, Chowdhury SR, Blank DHA. Micropor. Mesopor. Mater. 2003; 65:197–208.
44. Stöcker M. Micropor. Mesopor. Mater. 1999; 29:3–48.
45. Woodward CA, Dobson MP, Stace AJ. J. Phys. Chem. A. 1997; 101:2279–2287.

Highlights

- Ion exchange of Na-Y improves sorption capacity, adsorption heat and diffusivity
- Water uptake in small cages accounts for ~8.8% of the total uptake in the micropores
- Max. water uptake of 42.6 wt.% at 25 °C and 100% RP was predicted on Mg-Y (~70% IED)
- Addition of 20 wt.% methanol into water has no notable effect on overall performance
- Robust cyclic stability and lab-scale scalability were demonstrated

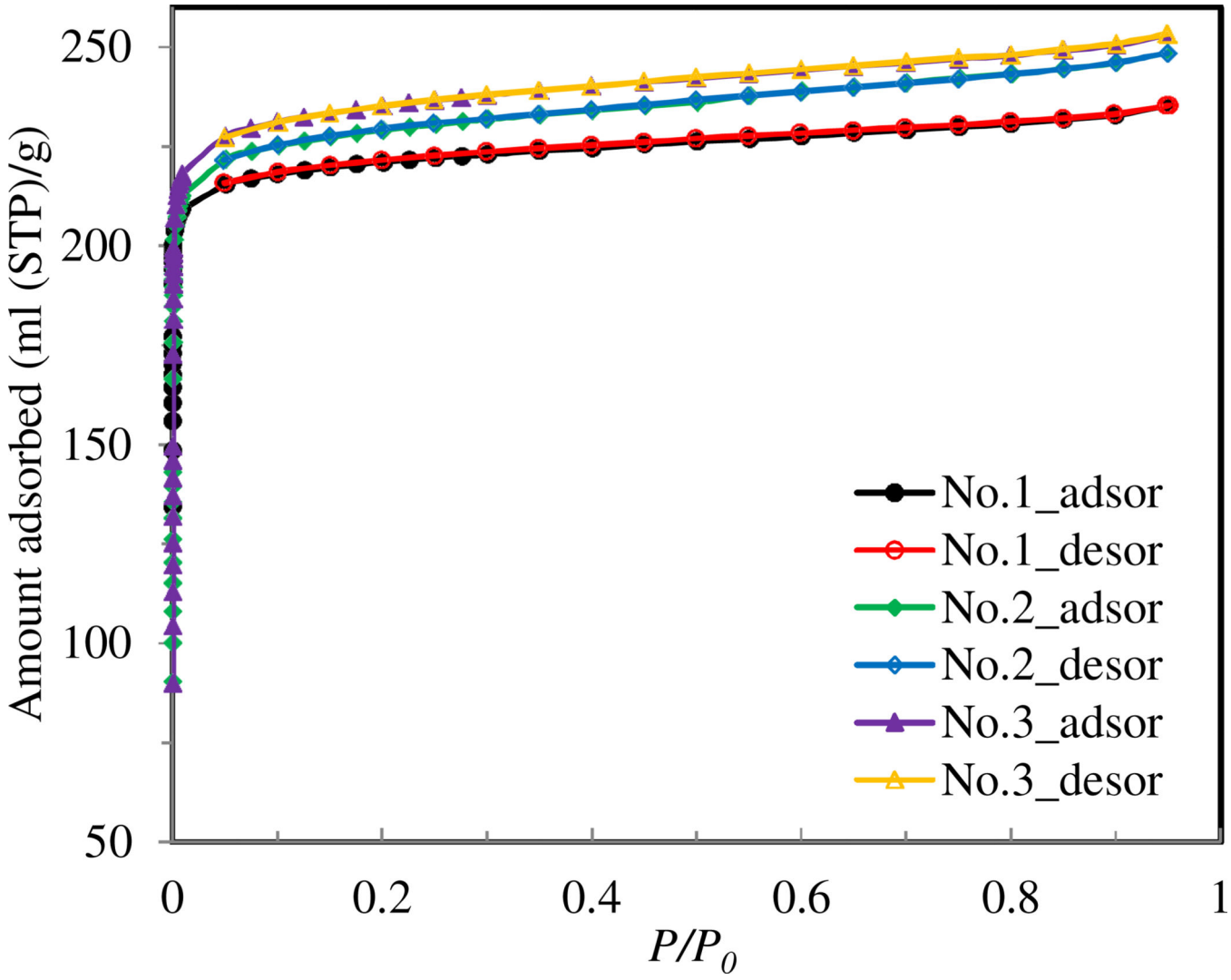

Fig. 1.

N_2 adsorption/desorption isotherms of the parent and modified Y zeolites at −196 °C.

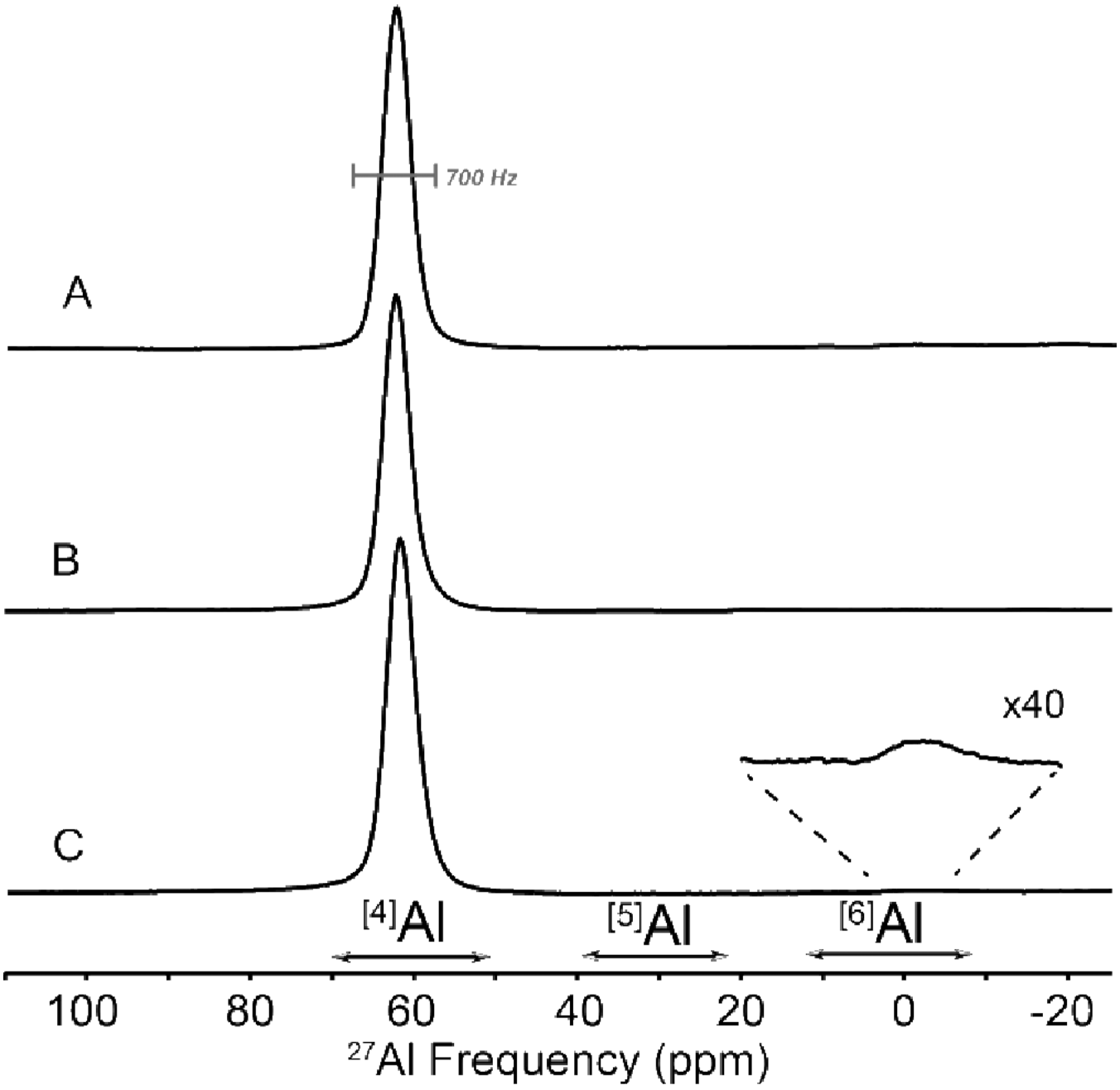

Fig. 2.
High-field (700 MHz, ^{1}H) ^{27}Al MAS NMR spectra of Y-type zeolites No. 1 (A), No. 2 (B) and No. 3 (C).

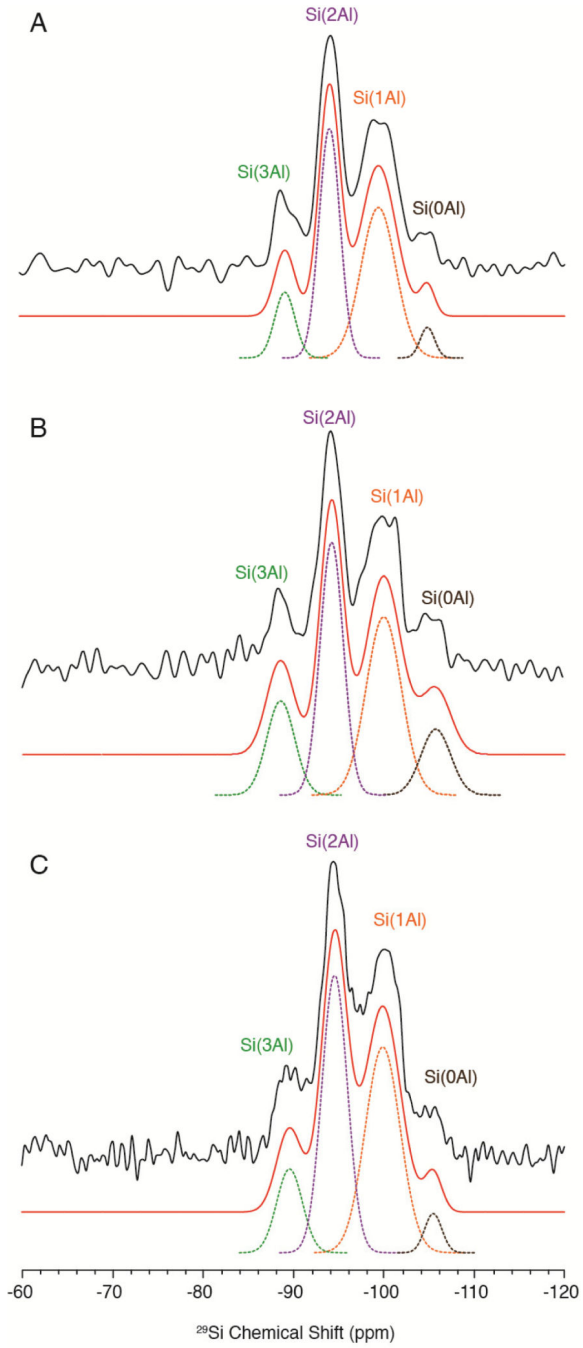

Fig. 3.

Experimental (black) and simulated (color) ^{29}Si MAS NMR spectra (400 MHz, ^{1}H) of Y-type zeolites No. 1 (A), No. 2 (B) and No. 3 (C). Overall fittings and individual deconvoluted peaks are shown as red and dotted lines, respectively.

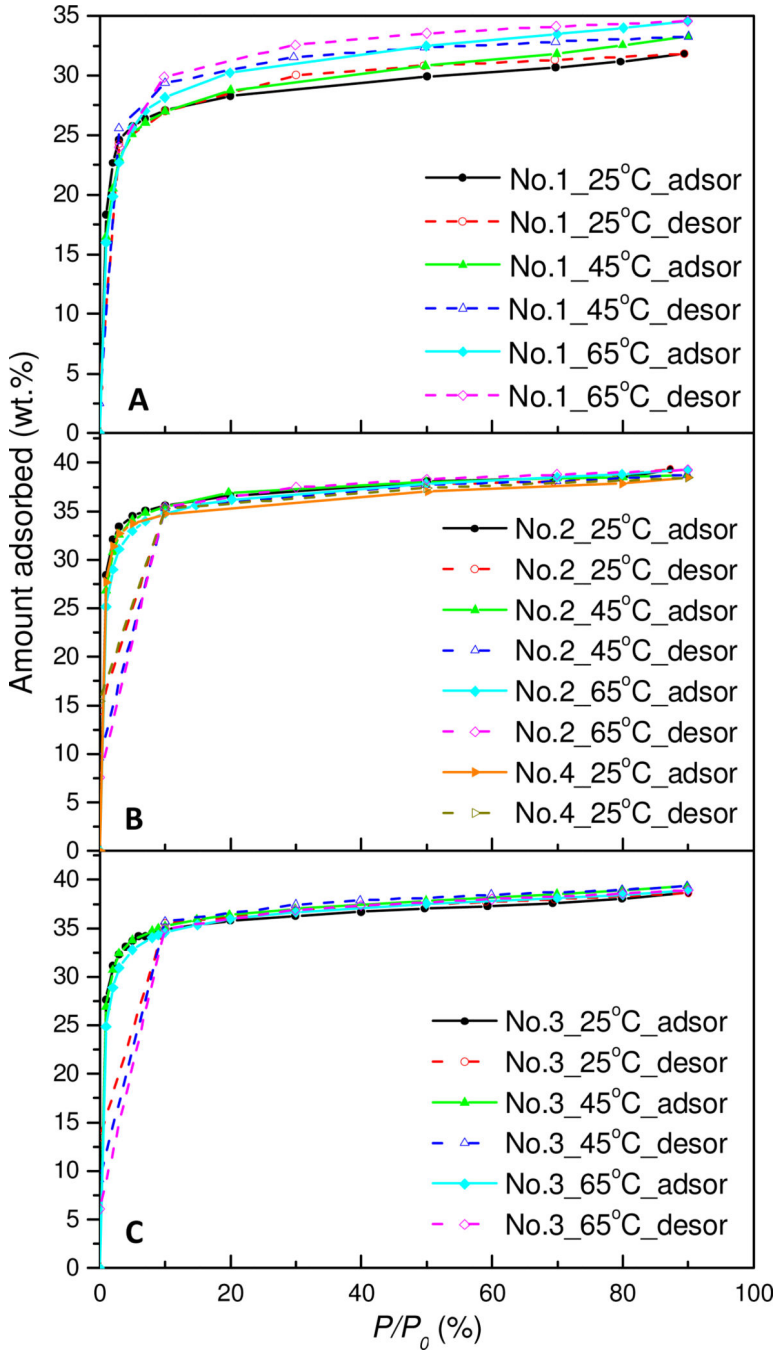

Fig. 4.

Water vapor adsorption/desorption isotherms of the zeolites No. 1 (A), Nos. 2 and 4 (B), and No. 3 (C) at 25, 45 and 65 °C. The dotted desorption trendlines are drawn to help guide the eye.

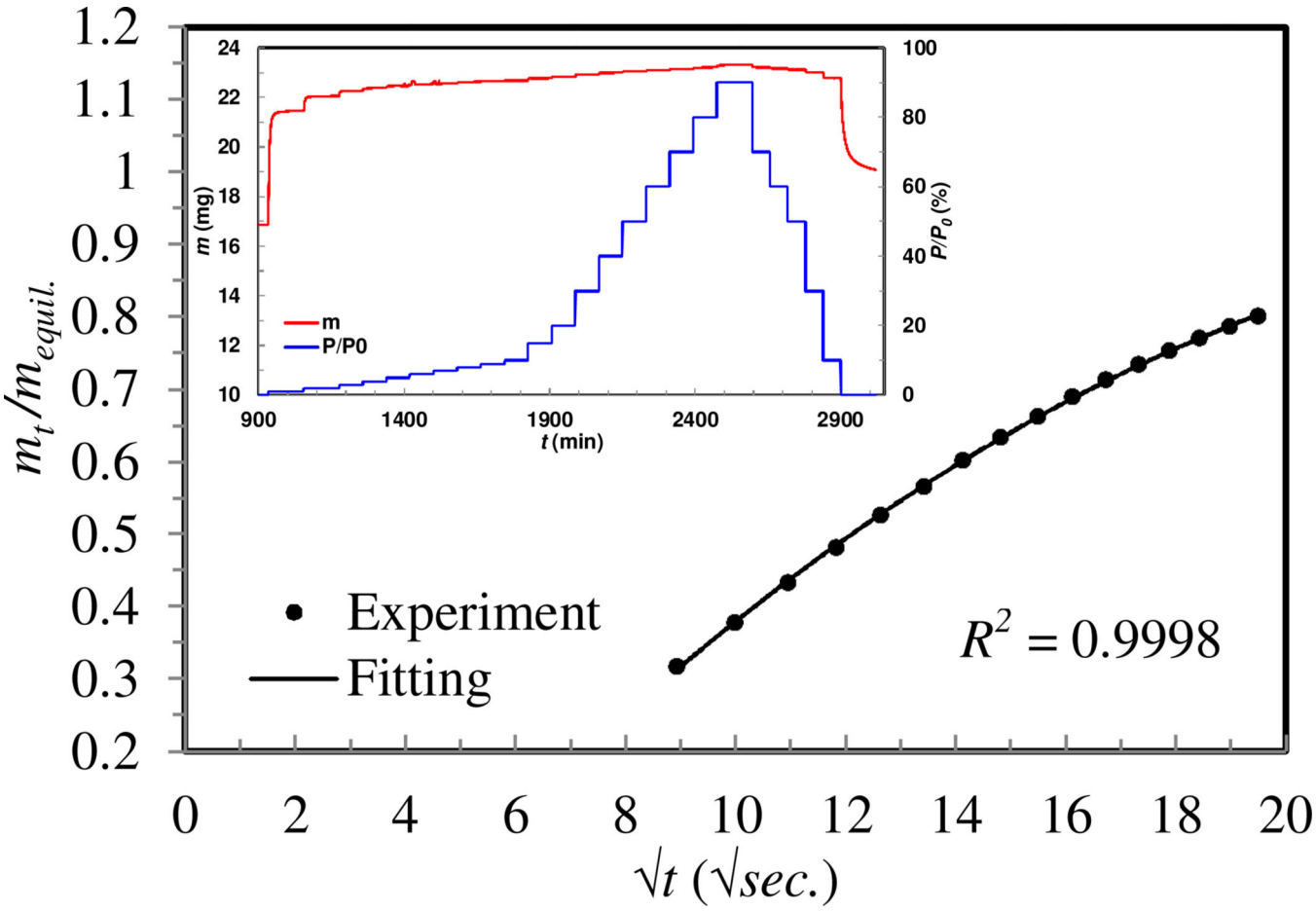

Fig. 5.

2nd-order polynomial fitting of $m_t/m_{equil.}$ vs. $\sqrt{t}$ using Eq. 5 on No. 3 for water vapor at 25 °C and 2% RP derived from the pre-degassed sample mass change in response to stepwise RP increment (inset).

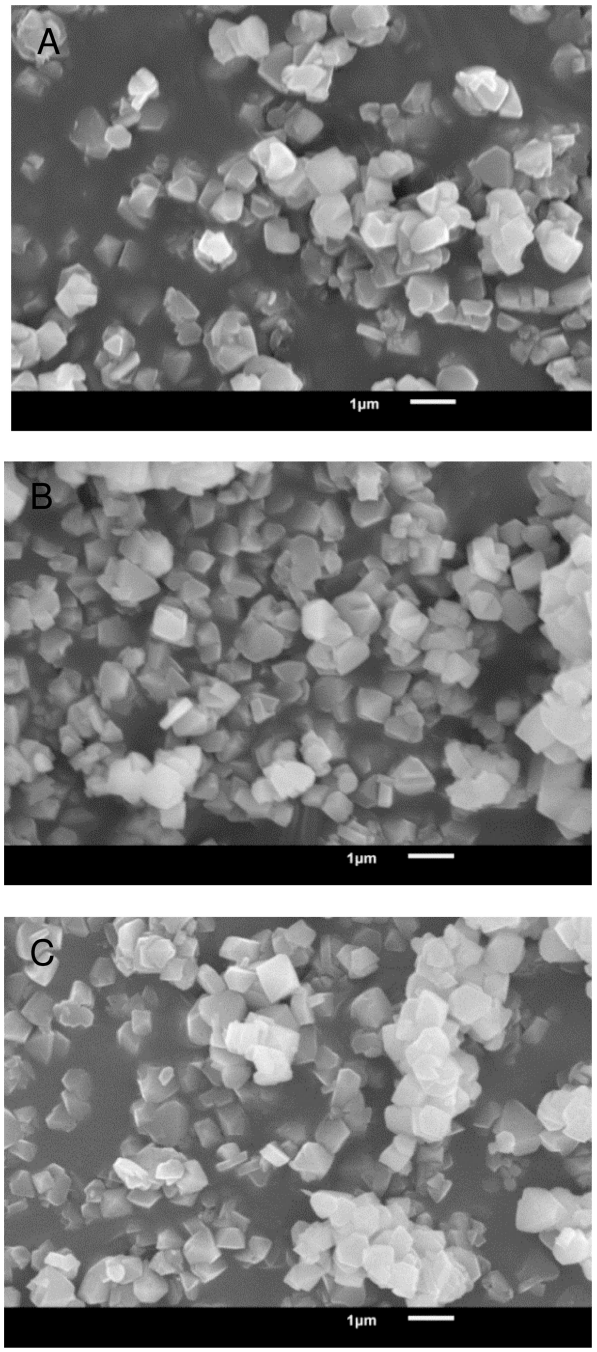

Fig. 6.
SEM images of zeolites No. 1 (A), No. 2 (B) and No. 3 (C) with all the scale bars of 1 μm.

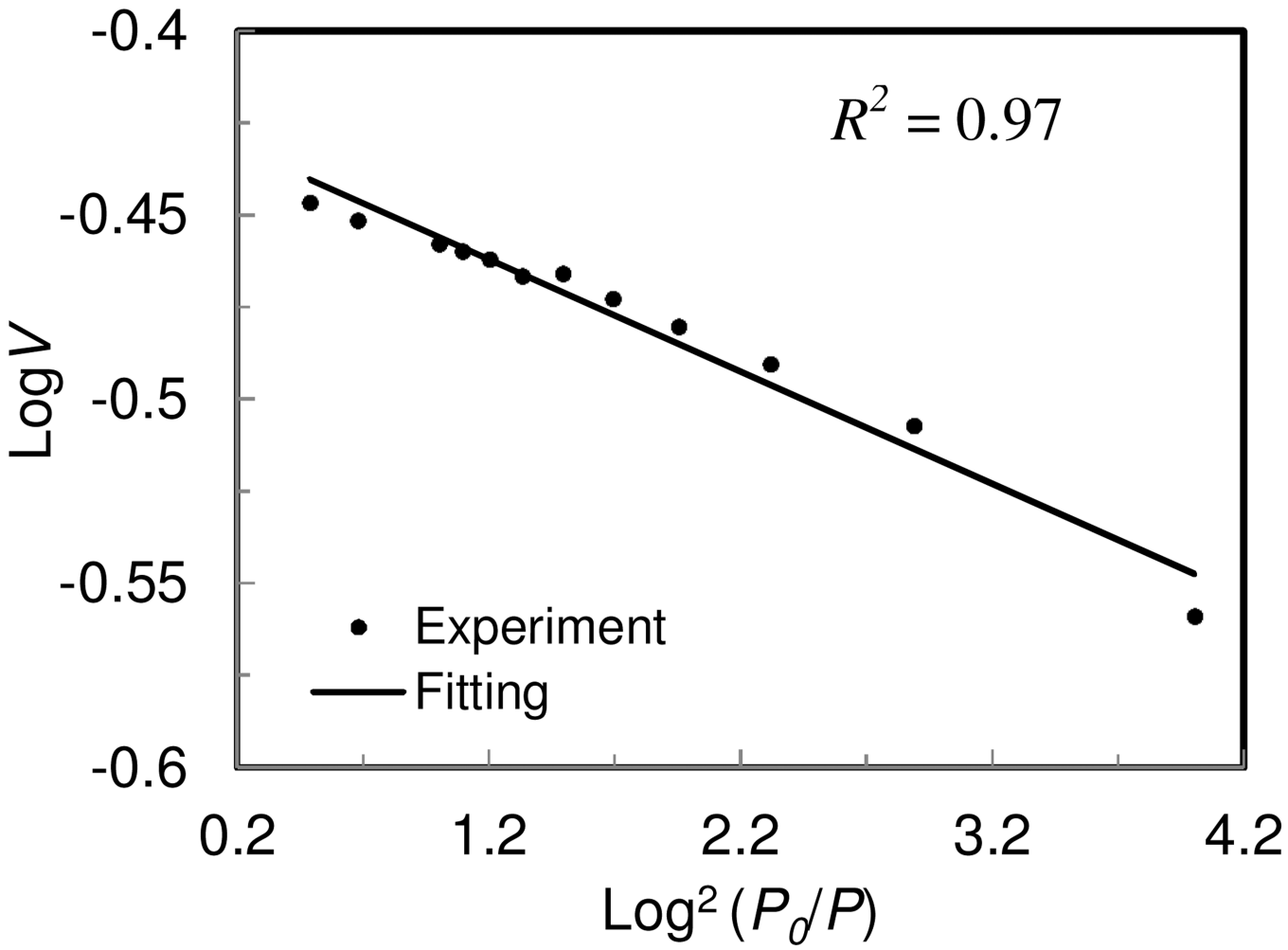

Fig. 7.
D-R plot of No. 3 at 25 °C for water vapor uptake.

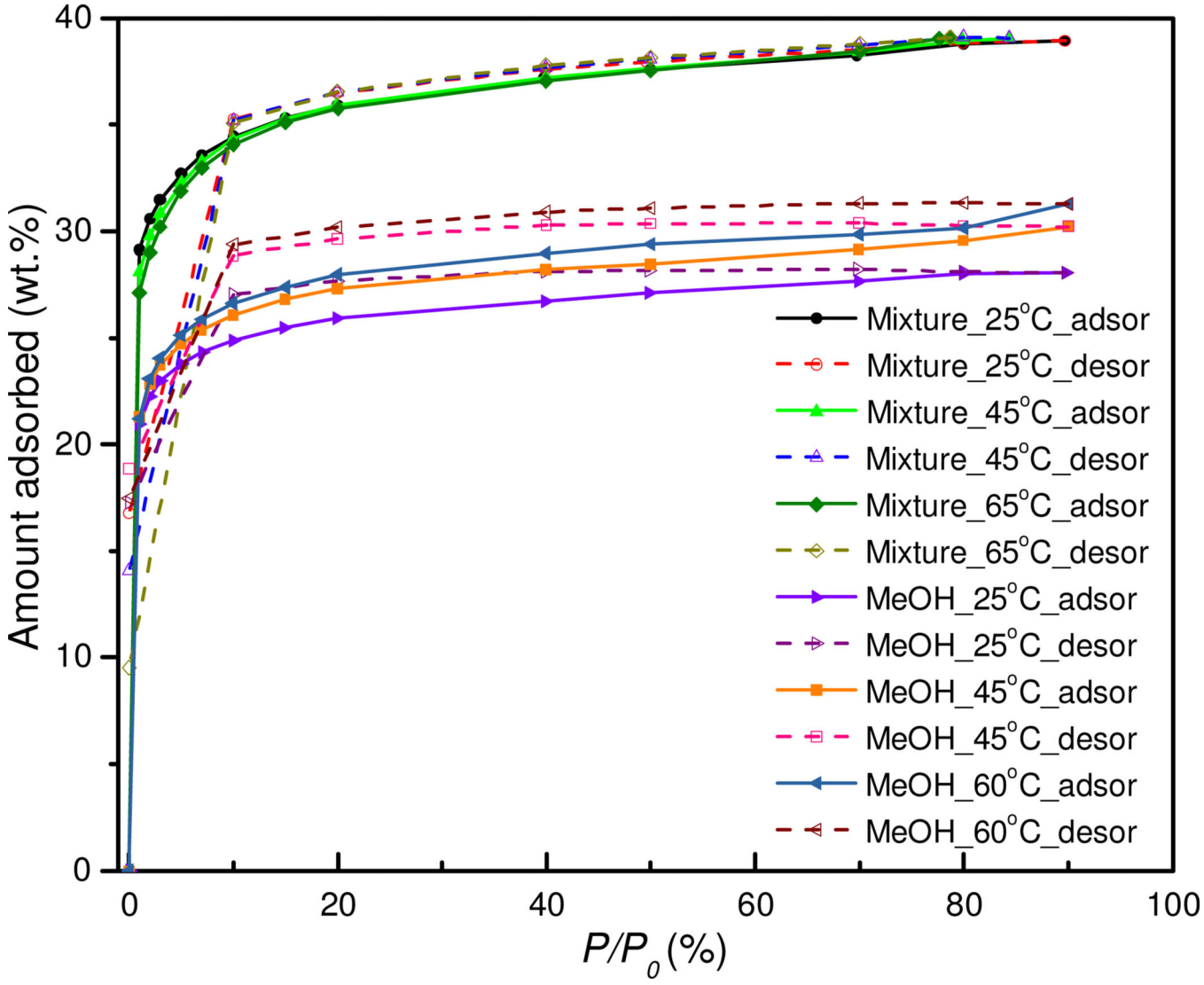

Fig. 8.

Total vapor sorption isotherms of No. 3 at varying *Ts* (25–65 °C) for 20 wt.% MeOH/H_2O mixture (A) and pure MeOH (B).

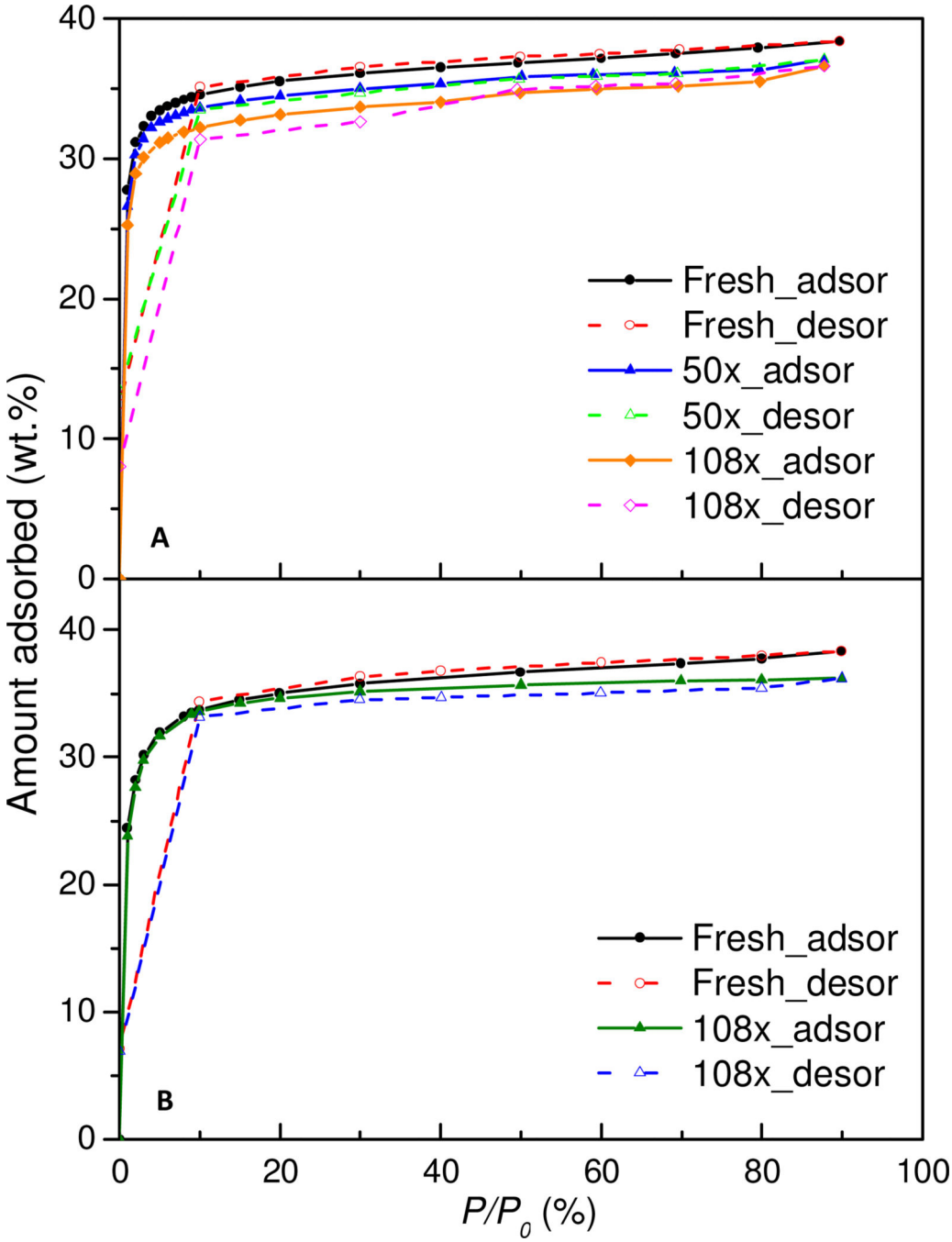

Fig. 9.
Water vapor sorption isotherms of No. 5 at 25 °C (A) and 65 °C (B) before and after multiple adsorption/desorption cycles.

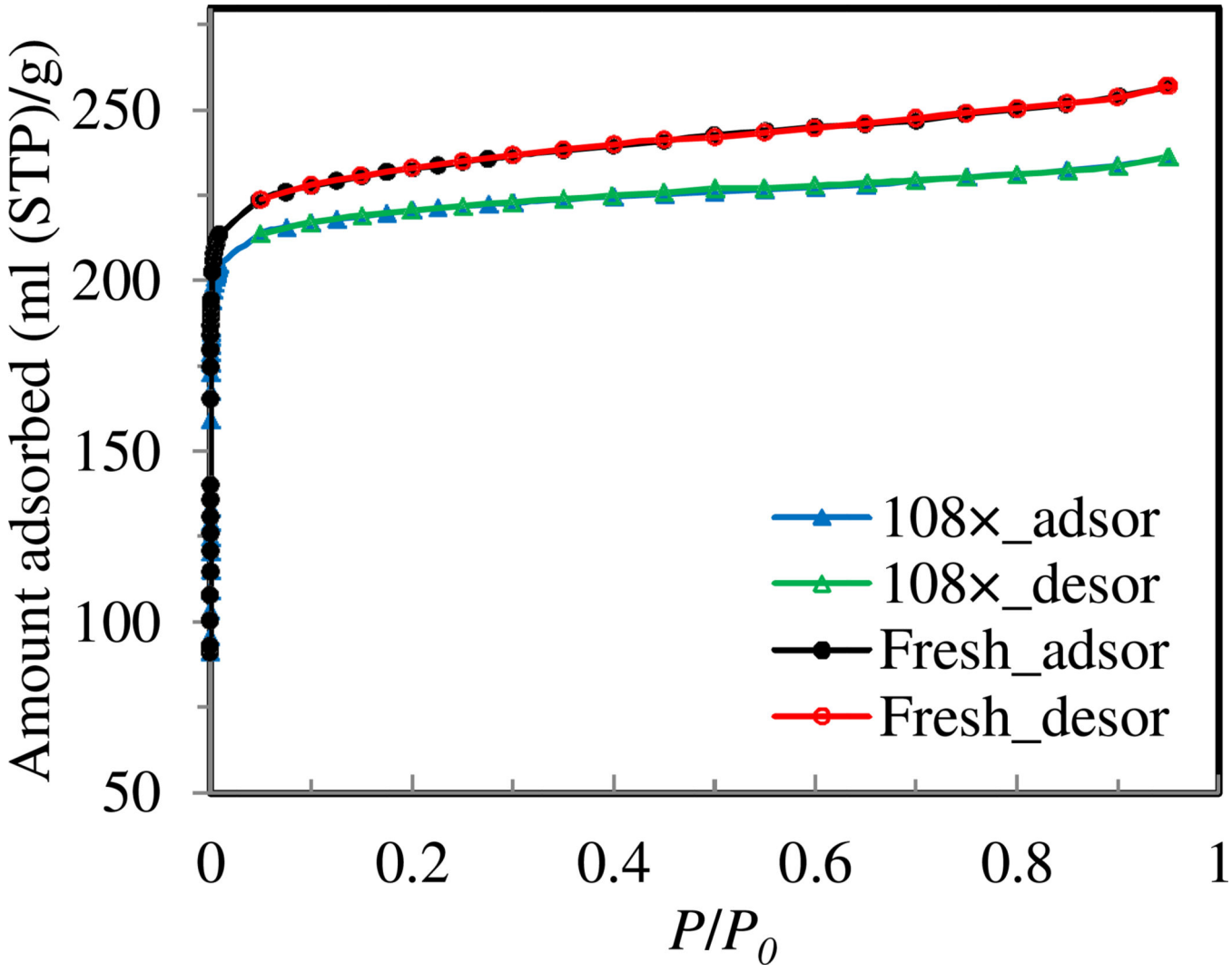

Fig. 10.

N_2 sorption isotherms of No. 5 before and after 108-fold cycles at −196 °C.

Table 1

Textural parameters determined by N_2 sorption for the parent and modified Y-type zeolites.

Sample	V_t (ml/g)	V_{micro} (ml/g)	S_{BET} (m^2/g)	S_{micro} (m^2/g)	$S_{external}$ (m^2/g)
No. 1	0.365	0.326	667.3	629.0	38.3
No. 2	0.385	0.333	694.1	642.6	51.5
No. 3	0.393	0.342	713.8	661.0	52.7
No. 5	0.398	0.330	710.4	638.8	71.6
No. 5_108× [a]	0.366	0.326	668.3	629.1	39.2

[a] Zeolite No. 5 after 108-fold adsorption/desorption cycles.

Table 2

Elemental composition and IED of the parent and modified zeolites determined by $^{29}Si/^{27}Al$ MAS NMR spectroscopy and ICP.

Zeolite	NMR data			ICP data			
	$(Si/Al)_{NMR}$	$^{[4]}Al$	$^{[6]}Al$	$(Si/Al)_{ICP}$	$(Na^+/Al)_{ICP}$	$(H^+/Al)_{ICP}$	IED (%)
No. 1	2.50	100%	0%	1.95	1.15	0	---
No. 2	2.54	100%	0%	2.09	0.359	0.028	64.1
No. 3	2.47	99.7%	< 0.3%	2.15	0.285	0.045	71.5

Table 3

Sorption capacity and *D* of the zeolites with and without tailoring for water vapor at different operating *Ts* and RPs.

Zeolite	*T* (°C)	Adsorption capacity (wt.%)		*D* at 2% RP (cm^2/s)
		2% RP	90% RP	
No. 1	25	22.66	31.79	7.06×10^{-13}
	45	20.51	33.28	9.96×10^{-13}
	65	19.84	34.56	1.13×10^{-12}
No. 2	25	32.09	39.28 [a]	9.14×10^{-13}
	45	30.76	38.73	1.09×10^{-12}
	65	29.02	39.24	1.25×10^{-12}
No. 3	25	31.97	38.97	1.94×10^{-12}
	45	30.71	39.32	1.99×10^{-12}
	65	28.86	38.91	2.46×10^{-12}
No. 4	25	31.35	38.44	9.04×10^{-13}

[a] The data was acquired at 87.3% RP.

Table 4

Adsorption properties of the parent and modified zeolites for water vapor based on the fitting with the D-R equation.

Zeolite	T (°C)	R^2	V_0 (ml/g)	E_0 (kJ/mol)
No. 1	25	0.94	0.309	−82.9
	45	0.98	0.320	−76.8
	65	0.99	0.342	−75.2
No. 2	25	0.96	0.384	−108.6
	45	0.98	0.391	−102.7
	65	0.99	0.386	−101.6
No. 3	25	0.97	0.375	−107.9
	45	0.98	0.383	−106.4
	65	0.98	0.384	−101.2

Table 5

Representative physical parameters of the adsorbates of interest.

Adsorbate	Saturation vapor pressure (P_0 in Torr)			Vapor composition (wt.% H_2O)			BP (°C)	FP (°C)	LHC [a] (kJ/mol)
	25 °C	45 °C	65 °C	25 °C	45 °C	65 °C			
H_2O	23.8	71.9	187.5	100	100	100	100	0	−40.7
20MeOH/80H_2O	44.9	128.9	320.3	35.8	39.0	41.7	86	−18	---
MeOH	126.4	332.6	629.4 [b]	0	0	0	64.7	−97.6	−35.3

[a] LHC: Latent heat of condensation;

[b] Data at 60 °C to prevent MeOH boiling at a typical *T* of 65 °C.

Table 6

Uptake capacity and *D* of No. 3 for 20 wt.% MeOH aqueous mixture and MeOH at different *Ts* and RPs.

Adsorbate	*T* (°C)	Adsorption capacity (wt.%)		*D* at 2% RP (cm^2/s)
		2% RP	90% RP	
$MeOH/H_2O$	25	30.59	38.94	9.55×10^{-13}
	45	29.77	39.06 [a]	1.04×10^{-12}
	65	28.99	39.09 [b]	1.53×10^{-12}
MeOH	25	22.25	28.06	---
	45	22.84	30.21	---
	60	23.08	31.28	---

[a] Data at 84.4% RP;

[b] Data at 78.7% RP.